Geocarto International

ISSN: (Print) (Online) Journal homepage: https://www.tandfonline.com/loi/tgei20

Geomorphological and anthropic impacts over land surface displacements: application of DinSAR technique to the case of Bahía Blanca city, Argentina

Nicolás Scivetti, Paulo Marcos, María Eugenia Prieto, Cecilia Pavón Pivetta, Leonardo Benedini, Agustín J. Stremel, Marcos E. Bahía, Andrés Bilmes & Sebastián Richiano

To cite this article: Nicolás Scivetti, Paulo Marcos, María Eugenia Prieto, Cecilia Pavón Pivetta, Leonardo Benedini, Agustín J. Stremel, Marcos E. Bahía, Andrés Bilmes & Sebastián Richiano (2021): Geomorphological and anthropic impacts over land surface displacements: application of DinSAR technique to the case of Bahía Blanca city, Argentina, Geocarto International, DOI: 10.1080/10106049.2021.1974960

To link to this article: https://doi.org/10.1080/10106049.2021.1974960

Accepted author version posted online: 30 Aug 2021.

Geomorphological and anthropic impacts over land surface displacements: application of DinSAR technique to the case of Bahía Blanca city, Argentina

Nicolás Scivetti[*1,2], Paulo Marcos[3,4], María Eugenia Prieto[5], Cecilia Pavón Pivetta[2,6], Leonardo Benedini[2,6], Agustín J. Stremel[2,6], Marcos E. Bahía[6,7], Andrés Bilmes[1], and Sebastián Richiano[1],

[1]Instituto Patagónico de Geología y Paleontología –IPGP- (CENPAT-CONICET), Puerto Madryn, Argentina

[2]Departamento de Geología, Universidad Nacional del Sur (UNS), Bahía Blanca, Argentina

[3]Universidad Nacional de Río Negro. Instituto de Investigación en Paleobiología y Geología, General Roca, Río Negro, Argentina

[4]IIPG. UNRN. CONICET, General Roca, Argentina

[5]Instituto de Diversidad y Evolución Austral (IDEAus). Centro Nacional Patagónico (CENPAT). Consejo Nacional de Investigaciones Científicas y Técnicas. CONICET

[6]Instituto Geológico del Sur (INGEOSUR), Universidad Nacional del Sur (UNS)-CONICET, Bahía Blanca, Argentina

[7]Departamento de Física, Universidad Nacional del Sur (UNS), Bahía Blanca, Argentina

*Corresponding author: nscivetti@cenpat-conicet.gob.ar

Abstract

This article analyses the Line of Sight (LOS) surface velocity for the 2016 − 2020 period, in Bahía Blanca city using DInSAR technique. The results show significant LOS velocities in determinate sectors of the city, presenting values of up to −20 mm/year. Based on the results, we divide the city into three different sectors as a function of LOS velocity, the urban growth factor, and the topographic slope. Sector A, where the subsidence is being induced by loads of new buildings, soil compaction and waterproofing, and residential groundwater pumping. Sector B, where the highest displacement rates are triggered by a combination between groundwater pumping and soil creep process. Sector C has the lowest velocities, low urban growth factor, and absence of groundwater pumping. In all cases, the surface displacement indicates that a review of the urban planning should be carried out as well as increasing control over the groundwater exploitation.

Keywords: subsidence rate, Soil creep, DInSAR, Argentina

1 Introduction

Surface subsidence is a major threat hazard in urban areas and human activities resulting in long-term economic losses linked to infrastructures damage; unfortunately, sometimes causing life losses in catastrophic events (e.g., Varnes, 1974 and Federico et al., 2012); and other environmental risks as for example increased flooding potential, salt water intrusion and landslides (e.g., Phien-wej et al., 2006; Koster et al., 2018; Ciampalini et al., 2019). Some of anthropogenic factors that could act as the main factor of the subsidence process in specific places are related to deficient building

planning and/or urban area expansion (e.g., Listo and Vieira; 2012; Abidin et al., 2013; Dang et al., 2014; Khorrami et al., 2020); mineral mining and hydrocarbon exploitation (e.g., Morton et al., 2002; Federico et al., 2012); subway, tunnels, bridges, and roads infrastructures developments (Osmanoglu et al., 2011; Zhang et al., 2018); and groundwater pumping (e.g., Phien-wej et al., 2006). On the other hand, geological settings linked to topographic-geomorphologic configuration; uplift rates in active tectonics settings; and soil features are some of the other variables that could influence the subsidence process (Carminati and Martinelli, 2002; Teatini et al., 2011; Fiorucci et al., 2011; Pawlik and Šamonil; 2018).

The overexploitation of the aquifer systems is one of the main land subsidence triggers in many populated cities and agricultural areas (e.g., Poland, 1984; Carminati and Martinelli, 2002; Phien-wej et al., 2006; Abidin et al., 2013; Chen et al., 2016; Koster et al., 2018; Khorrami et al., 2020) producing the compactions of soils in regions with heavily dependent on groundwater supplies. This water extraction could results in permanent land subsidence. On the other hand, the load of the new buildings generates soil compaction, causing land subsidence, and leading to severe damage if the buildings lack adequate foundations (Peduto et al., 2017; Stramondo et al., 2008).

Another problematic scenario comes from the soil creep process that can affect buildings located on slopes. Soil creep affects the most superficial part of the surface and it is typically characterized by variable displacement ratios, from mm/year up to 0.1 m/year (Highland and Bobrowsky 2008). Buildings and infrastructure founded over zones with soil creep processes, can develop cracks, curved walls, and others damaged features. Over time, the degradation will eventually affect the structural stability and, therefore, the functionality of buildings and infrastructure (Crosetto et al. 2018).

Interferometric Synthetic Aperture Radar (InSAR) is widely used to map land subsidence over wide regions with high spatial-temporal resolutions (Chen et al. 2016). DInSAR (Differential InSAR) technique uses the SAR phase that is sensitive to the terrain topography and elevation changes occurring between two satellites passes over the same area. If the terrain topography is known (for example with a Digital Elevation Model [DEM]), the corresponding phase component can be subtracted from the InSAR phase, leaving the component related to the deformation of the terrain. This makes it possible to detect subtle deformations of the Earth's surface (Biescas et al. 2003; Sillerico et al. 2010).

This article aims to quantify the land surface displacement in Bahía Blanca city, to determine its spatial distribution using DInSAR technique, and latterly identify the major driving mechanisms. This contribution analyzes an example of urban building problems related to a complex relationship between human developments and geological-climate natural scenario.-The obtained results allow us to identify the potential subsidence cause and provide an important procedure to apply in future building planning to avoid a complex natural-anthropogenic configuration scenario.

2 Study area

Bahía Blanca city is located in the southwest of the Buenos Aires Province, Argentina (Fig. 1a and 1b) and constitutes one of the most crowded port Atlantic coast cities of the country with about 300.000 inhabitants. Climatically, the city presents an Atlantic regime with an average annual rainfall of 600 mm (Krepper et al. 1989), and is one of the most water-stressed cities in Argentina.

Since its foundation the city has experienced problems related to the water supply. Various infrastructure works and projects were proposed and developed to provide the city with water from surface runoff, without concrete solutions. These phenomena, added to the existence of a deficient drinking water network that supplies part of the city (Fig. 1b), increase the groundwater extraction,

without regarding control the number of pumping boreholes, their location or distribution, or the groundwater volumes extracted.

Since 2001, the city of Bahía Blanca presents a significant expansion of the urban area combined with a lower level of population (Fig. 1c, 1d, and 1e). Taking into account that the city periphery is expanding quickly in a non-regulated way (CIPPEC 2017), the occupation of geotechnical and environmentally unfavourable spaces such as floodplains or unsuitable foundation soils could be occupied.

2.1. Topography, geology and geomorphology

The urban area of Bahía Blanca city is located at two topographic levels, each of them with a low slope (<0,5%). The higher topographic level presents values between 50 and 80 m above sea level (asl) and the lower one presents values between 0 and 20 m asl (Gentili et al. 2020). Both levels are connected through a topographic surface with NW-SE strike direction and a southwest slope ranging between 2% and 5% (Fig. 2a). The stratigraphy include Paleozoic deposits, associated to a basin developed over a Paleoproterozoic - Middle Cambrian basement (Rapela and Kostadinoff 2005; Tohver et al. 2012; Folguera et al. 2017), which reach a thickness of around 5100 m (Folguera et al. 2017). The Cretaceous deposits are dominated by coarse continental to shallow marine sandstones and conglomerates (Franke et al. 2006). Finally, a set of Paleogene, Neogene and Quaternary deposits complete the stratigraphy of the area (Folguera et al. 2017).

The landscape of the study area is represented by alluvial-colluvial deposits and colluvial plains, together with actual and ancient tidal plains, and littoral cords (Fig. 2b). The first are found in present rivers and creeks. Active tidal flats are constituted of unvegetated clay deposits defined as an albufera environment (Benedetti 1997). The ancient plains develop towards the interior of the coast, and are currently affected by water erosion and covered with vegetation, while the coastal chords show the transgressive-regressive processes that occurred during the middle-late Holocene (Folguera et al. 2017) (Fig. 2b).

2.2. Soils

In the study area, there are mainly two edaphic Orders: Mollisols and Entisols, while the Aridisols are scarcely represented. Certain subgroups of soils predominate in all of them (Folguera et al. 2017) (Fig. 2c).

a) Typic Haplustolls: These soils subgroups correspond to Mollisols Order and to the Ustolls Suborder. Around the study region, they are well-drained, develop silty-clay loam texture, and have a petrocalcic horizon that frequently constitute a diagnostic characteristic. For these reasons, at about five kilometers to northeast limit of the study area, Blanco et al. (2003) classified the soil as paleustolls petrocalcic. Another Ustolls subgroup soils were recognized by Blanco et al. (2003) in the region, but they are placed far away from our study area. Take into account the nearest location, we considered that the petrocalcic paleustolls with profile succession of horizons A-AC-Ck-2Ckm (Blanco et al. 2003) is probably the most representative soil of the Bahía Blanca´s building foundations (Fig. 2c). Horizon A and AC achieves around 50 cm thick and contain organic matter, while the Ck has pieces of evidence of secondary calcite belongs to the petrocalcic horizon (2Ckm) located at 80 cm depth.
b) Aquic Ustifluvents: These soil subgroups correspond to Entisols Order and to the Fluvents Suborder. They are represented in the littoral zone, where the salt flats dominate a landscape formed by extensive plains and tidal channels (Fig. 2c). They are flooded soils poorly drained where genetic

horizons have not developed. There are only sediment layers differentiated by color, degree of hydromorphism, and content of concretions.

c) Calcic Aquisalids: These soil subgroups correspond to Aridisols Order and to the Salids Suborder. They are restricted near to the Bahía Blanca estuary coast and developed in ancient plains of marine influence (Fig. 2c). Soils present poor drainage, high water table and saline-sodium characteristics. These are flooded soils that are typically constituted by a sequence of three horizons. The superficial horizon has sandy loam texture and little organic matter and saline efflorescence, while the subsurface ones have sandy clay and calcium carbonate as concretions and powdery.

2.3. Hydrogeology

The hydrogeological units of the study area can be synthesized as follows (Table 1 - Carrica et al. 2020):

The hydrogeological basement is composed of the crystalline basement rocks and the Paleozoic sedimentary cover with mainly aquifuge characteristics, but with low secondary permeability degree generated by a fractures system. The Hypoparanian section includes the Fortín (aquifuge behavior), Colorado (aquifer behavior), Pedro Luro (aquiclude behavior) and Ombucta (with aquitard-aquiclude characteristics) Formations. The Paranian section is represented by the Barranca Final Formation forming an aquiclude environment with some aquifer intercalations presenting high salinity waters. The Epiparanian section is composed of the Cerro Azul Formation with an aquifer level and brackish waters at the base and forming the free aquifer to the top. However, it presents frequent local hydrolithological anisotropies giving rise to an alternation of aquifer-aquitards levels.

In the study area, the phreatic aquifer is located at different depths depending on the geomorphologic conditions. In the northwest sector of the study area, the saturated zone is around 20 m depth; while it crops out in surface near the estuary zone (Carrica et al. 2020). Chemical parameters affect the groundwater quality in the urban area of Bahía Blanca (dissolved salt, and locally sewage waste contamination). In contrast, the aquifers located in peripheric areas contain excellent chemical and physical parameters for human supply (Bonorino et al. 2009). Pumping tests, at the constant flow rate, carried out in the first 100 m of saturated thickness, yielded average transmissivities of 144 to 230 m2/d, and storage coefficients of 0.1, with delayed drainage (Albouy et al. 2005; FUNS 2000).

Concerning surface runoff, there is the Napostá Grande Creek. This creek is the mainstream that presents an effluent and permanent regime like most of the streams of Buenos Aires´s province (Albouy and Bonorino 1997) with a flow of 86400 m3/d (Carrica 1998). However, it should be noted that the Napostá Grande Creek is piped for most of its route through the city of Bahía Blanca, losing its effluent regime.

3 Methodology

3.1. Line of Sight (LOS) velocity maps

In this contribution, we use Sentinel-1 mission images for mapping and monitoring the surface deformation. The Sentinel satellite constellation series, developed by the European Space Agency, represents the dedicated space component of the European Copernicus program, committed to long-term operational services in a wide range of application domains (Nagler et al. 2015).

The dataset used in this study consists of thirteen images from Sentinel satellite constellation acquired from 2016 to 2020; downloaded from the Copernicus Open Access Hub (https://scihub.copernicus.eu/dhus/#/home) collected from descending track with VV polarization. The September 20th, 2016 acquisition was selected as the master scene. The interferograms were generated from single-look complex (SLC) images using SNAP version 7.0.4 software. The external Shutter Radar Topography Mission DEM with 90 m resolution was used to remove the topographic component of the interferometric phase and geocode the interferograms.

The methodology steps were based on Serco Italia SPA (2018) and Braun and Veci (2020) applied to the land subsidence and interferometry, as follows: a) Data download. b) Open and explore data: to verify that the images are adequate and to check the integrity of the data. c) Pre-processing: to select the sub-swath and the bursts of the interest area avoiding processing the entire image. d) Co-registration: to provide accurate satellite position and velocity information. e) Interferometric processing: to produce an interferogram between the interferometric pairs (master and slave images) including a coherence image estimation. f) Phase Unwrapping: to be able to relate the interferometric phase to the topographic height. g) LOS displacement map: to convert the interferometric phase to displacement and to produce the displacement product for each interferometric pair:

$$\text{Displacement} = (\text{unwp} * \lambda)/(-4 * \pi)]$$

Where unwp is the unwrapped phase, λ is the wavelength and π is the mathematical constant.

h) Moreover, the average coherence was also calculated. A new valid pixel expression was entered for the total displacement band (for instance average coherence > 0,4). By averaging the coherence of several dates, the impact of atmospheric disturbances and unwrapping errors was reduced, and actual displacement patterns become more evident. However, this assumes that the deformation trend is linear between the first and the last image pair (Braun and Veci 2020). i) Geocoding: to compensate for topographical variations of a scene and the tilt of the satellite sensor distortions.

The resulting Line of sight velocity map (in mm/y units) was overlaid on Google Earth imagery. Finally, four cross sections were made in different sectors of the city to compare and analyse the relationship between the LOS velocity and the topography. For this, the cross sections were designed perpendicular to the greatest topographic slopes.

3.2. Line of Sight (LOS) velocity by neighbourhood

Once the LOS surface displacement velocity was obtained, an average value was assigned to each neighbourhood of the city based on the values presented inside each polygon, to visualize and interpret the displacement distribution in a more expeditious way. This was carried out using the Zonal Statistics tool available in QGIS 3.16 Hannover software. This tool allows for analysing only polygon-type entities and it allows obtaining information such as the number of pixels, the mean minimum, and maximum pixel values, among others, for each polygon contained in the vector layer.

3.3. Urban footprint

The magnitude of the interferometric coherence can be used to detect changes in the observed target over the time between two acquisitions (Koppel et al. 2015). Natural targets tend to lose coherence faster than non-natural targets, giving rise to the use of the coherence parameter for detecting built-up areas (Strozzi and Wegmuller 1998).

Sentinel 1 SLC images were used to mask the urban footprints in 2016 and in 2020 to obtain the growth of the urban area in the mentioned period. The methodology follows the step-by-step procedure proposed by EO-College - European Space Agency (ESA), according to four stages: 1) Calculation of backscatter intensity from a Single Look Complex (SLC) data set. 2) Calculation of the interferometric coherence of two SLC data sets. 3) Create an RGB composite using backscatter and coherence layers. 4) Mask out the urban footprint. Finally, a comparison was made between both images to determine the expansion of the urban footprint in each neighbourhood. The obtained urban growth factor, which was calculated using the difference between 2016 and 2020 footprint, expresses the neighbourhood buildings increase in the analysed period.

3.4. Slope map

To analyse the distribution of topographic slopes in the study area and its relationship with the LOS velocity, a slope map was constructed from the digital elevation model (DEM). Map processing was carried out using the Slope tool of QGIS 3.16 Hannover software, configured to return the results in angular degrees.

4 Results

4.1. Los velocity map

The LOS velocity map of the Bahía Blanca city with a coherence major or equal to 0,4 is shown in Figure 3. A significant data set —showing on the map— present a coherence greater or equal to 0,4; giving good reliability to them (CCRS 2000). The map also shows that the magnitude of the LOS values is not distributed randomly. The main distribution pattern of the LOS velocity shows a value differentiation in the NW-SE trend. The lower displacement values occur in the southwest segment (with values ranging from 0 mm/y up to −10 mm/y) while higher at the northeastern one (reaching values up to −20 mm/y), indicating a progressive growth towards the NE region (Fig. 3). However, locally, the LOS velocity distribution does not follow this pattern, e.g., in the north region, next to the Napostá Grande Creek, relatively low values are recorded (ranging from −10 mm/y up to −12,5 mm/y).

Table 2 shows the ID, the surface, the number of pixels within each polygon, and the mean and maximum values of LOS velocity for each neighborhood of the Bahía Blanca city. In the analyzed period (four years), the LOS displacement present values between 0 mm/y and −20 mm/y, and we grouped and divided them into three categories. Low LOS velocity (0 to −6.66 mm/y) values, medium LOS velocity (-6.66 to −13.33 mm/y) values, and high LOS velocity (-13.33 to −20 mm/y) values. Considering a total analysed surface of 87.42 km2; the results indicate that 42.67% of the area presents low LOS velocity values, 44.56% presents medium LOS velocity values, and 12.23% presents high LOS velocity values.

Figure 4 shows the mean value of LOS velocity for the neighbourhoods circumscribed by each polygon. Although some information could be lost when discretizing the LOS velocity values for each polygon into a single value, it is useful to get an expeditious interpretation of the LOS velocity at each neighbourhood. From the map in Figure 4, it is possible to identify that the neighbourhoods located in the central, north, northeast, east, and southeast sectors of the city are those with the highest values of LOS velocity (red, pink, and purple colours). The sectors located approximately in the northwest and south-southeast show mean LOS velocity values (orange colour). The sectors with the lowest LOS velocity values are located in the west, southwest and south of the study area (yellow colour).

4.2. Los velocity and urban growth

Before to analyse the linkage between the LOS velocity and the urban growth, we needed to stablish the urban growth factor for each neighbourhood of the study area (Table 2) (Fig. 5). The obtained values range from 1 up to 1.22 (0% up to 22%) and allow to create the urban growth factor map (Fig. 5). Figure 5 distinguish a random distribution of the neighbourhood's urban growth rate. For this reason, there is no delimitation pattern of the city sectors with different rates of urban growth, being possibly conditioned by the space availability, preferences, social and economic capacities.

A direct relationship between the LOS velocity (Fig. 4) and the urban growth factor (Fig. 5), is not appreciable at first glance. The analysis of the correlation factor allows evaluating the degree of linkage between the mentioned variables. The result of the correlation coefficient is −0.1018, which shows a very low negative correlation (Fig. 6a). However, existing neighbourhoods in the city have experienced relatively high LOS velocity values (> 13.6 mm/y) and high urban growth factor (> 1.10) (Fig. 6b).

4.3. Los velocity and topography

The relationship between the LOS velocities and the topographic features of the study area was analysed using a slope map, four topographic-LOS values cross-sections, and comparing LOS displacement velocity against the Mean topographic slope (Fig. 7 and 8a). The LOS velocity intervals distribution and the slope map obtained by the digital elevation model (DEM) of the study area is shown in Figure 7a. The slope map shows topographic gradients values ranging from ≈ 0° up to 5° with the higher slope values distributed with an NW - SE trend displaying the greatest slopes in the north, central, as well as in southeast regions (Fig. 7a). Other high slopes are linked to the Napostá creek valley in the northeast area, but this region is placed outside of the Bahía Blanca buildings. Radomly and isolated high topographic slops could be distinguished near the south perimeter of the Bahía Blanca city.

The LOS velocity intervals (low-medium-high) and topographic cross-sections are shown in Figure 7b. All of the cross-sections show a direct relationship between the topography and LOS velocity in absolute values terms (Fig. 7b). The A* - A section shows topographic values from close to 0 m asl in the southwest sector up to around 73 m asl in the northeast sector, connected by a narrow high topographic slope zone. The LOS velocity values range from close to 0 mm/y up to around −20 mm/y, and the maximum LOS values location is coincident with the high topographic slope zone (Fig. 7a). The B* - B section shows topographic values from close to 0 m asl in the southwest sector up to around 50 m asl in the northeast sector, with a central sector reaching up to 75 m asl. The highest slope is located in the central-southwest sector, connecting topographic altitudes of 20 m and 75 m. The LOS velocity values reach around −20 mm/y and are correlatable with the highest topographic values but also with the highest topographic slope (Fig. 7a, b). The C* - C section shows topographic values from close to 0 m asl in the southwest sector up to around 50 m asl in the northeast sector, with a central-northeast sector reaching up to 70 m asl. The LOS velocity values reach around −20 mm/y and are correlatable with the topographic slope break zone (Fig. 6a). The D* - D section shows topographic values from close to 0 m asl in the southwest sector up to around 75 m asl in the northeast sector, showing the most uniform topographic slope (Fig. 6a). The LOS velocity values reach around −20 mm/y and are correlatable to the beginning of the topographic slope break zone.

On the other hand, LOS velocity values against mean topographic slope values (Fig. 8a), also presents a certain degree of correlation. The degree of linkage between the aforementioned variables was also developed by the correlation factor. The correlation coefficient (-0,3944), shows a medium

negative correlation (Fig. 8a). A direct relationship between the LOS velocity and slope values is appreciated in some particular neighbourhoods (Fig. 8b).

The slope map and the cross-sections show that sectors with a relatively high topographic altitude and low slope (≥ 50 m; < 1°), correspond to the high LOS velocity category (up to −15 mm/y). However, the highest LOS velocity values are associated with the higher topographic slope areas (≈ 5°), where the LOS velocities reach up to −20 mm/y (Fig. 7a). Various neighbourhoods reflect this last combination for both variables (Fig. 8b). On the other hand, most of the low LOS velocities are registered in regions where the low topographic level and low slopes values prevail.

5 Discussion

5.1. Los velocity and topography

To understand the subsidence behaviour for the 2016 − 2020 period over the geomorphologic evolution of Bahía Blanca city, we evaluate the land surface displacement taking into account the soil type; phreatic aquifers; urban growth rates; topographic relief, and its slope values.

The soil types distribution of the study area shows that almost the entire building constructions are founded in the same soil type (Fig. 2a). For this reason, we avoided analysing this parameter because we understand that it could not explain the LOS velocity differences. In the same way, the stratigraphy beneath of the study area and the different geomorphic landscapes seem to have no influence on the variation of LOS velocities (Fig. 2b).

In a similar way, the urban growth factor variable recorded along the different neighbourhoods does not show a direct and clear relationship with the LOS velocity (Fig. 3, 5 and 6a). In contrast, a detailed topographic slope analysis shows a better relationship with the LOS velocity and topographic relief (Fig. 3, 7 and 8a). It allows us to consider the natural topographic relief such as a first-order factor that controlled the behaviour of the land surface displacement.

In sectors with topographic slopes lesser than 1°, the LOS velocity values are more representative of the vertical component movement than LOS velocity values obtained for higher slope sectors (2 − 5%), where the horizontal component could be considered greater (Manzo et al. 2006).

The north, northeast, and east sectors of the city are classified as LOS displacement medium category (from −10 up to −15 mm/y). They present a heterogeneous urban growth factor during the analysed period (Sector A – Fig. 9a), and constitute urban areas developed mainly in the last decade. In turn, these sectors located on a high topographic level (> 50 m) and very low slopes (<1°) are commonly supplied with consumption water through groundwater pumping. In this context, it is feasible to infer that the relatively medium to high values of LOS velocity is associated with the compaction of the subsurface soil triggered by the increased load generated by new buildings; waterproofing of the surface, and groundwater pumping (Foster et al. 1999; Stramondo et al., 2008; Catalao et al. 2012; Yang et al. 2018; Poreh et al. 2021).

The northwest, centre, and southeast sectors (Sector B – Fig. 9a) are those with the highest LOS velocity values (up to −20 mm/y), also with heterogeneous urban growth factor values. This sector (Sector B) is located in the area with the highest topographic slope in the city (reaching values that can exceed 5°). Although only the northwest and southeast sectors obtain water for consumption from groundwater pumping, the central residential sector uses this type of water for the maintenance of green spaces and for swimming pools. Given that irrigation can increase the percentage of

moisture on soils with different clay contents, it can generate the decrease its viscosity (Lohnes et al. 1972; Oehm & Hallet 2005; Liu et al. 2013) and to promote the creep processes. Therefore, the highest LOS velocity values obtained for Sector B could arise from the combination of groundwater extraction and the action of soil creep processes.

The west, southwest, and south sectors of the city (Sector C — Fig. 9a) are those with the lowest LOS velocity values (between 0 and 6,66 mm/y) and also heterogeneous urban growth factors. They are located on a low slope topography (<1°) and mostly have a water network supply. In this way, the low LOS velocity values could be linked to the scarce increase of loads and waterproofing of the surface associated with urban growth, the absence of soil creep processes due to the low topographic slopes and a reduced exploitation of groundwater.

5.2. Natural and anthropogenic controls

The natural geomorphologic configuration of the study area and the anthropogenic activities exert a combination that produce the land subsidence. Depending on the sector considered within the study area, the displacement driving mechanisms could correspond to subsidence and/or soil creep processes. Natural topographic slope develops an important factor in areas where the soil creep process prevails, even more when the anthropogenic factors could increase the moisture content of soils with clay containing. It is necessary to remark that the boundary of the area affected by soil creep cannot be defined using geomorphologic criteria alone (Crosetto et al. 2018). On the other hand, the over-pumping of the phreatic aquifer; the load, and surface waterproofing generated by new buildings during the urban growth corresponds to the human factor impact into the soil displacements. In this context, isolating the driving mechanism for each individual sector is a complex and challenging task. This study remarks that rigorous monitoring of subsidence and conscientious planning of the city urban growth is necessary on the higher topographic slope areas, due to this geomorphologic configuration contributes as soil creep trigger and because its natural behaviour cannot be avoided or solved. On the other hand, awareness and control over the extraction of groundwater directly linked to human activities and particularly in the high topographic sector of the study area, are essential to mitigate the effects associated with soil subsidence and its implications on buildings and the environment.

6 Conclusions

Bahía Blanca city shows LOS surface displacement velocities from 0 mm/y to up to −20 mm/y for the 2016 − 2020 period, which represents a maximum subsidence of about 8 cm in the last four years. The pattern of these results along the study area allows differentiating three major LOS intervals with low, medium and high values developing segments with NW-SE trend direction. We matched these results with neighbourhood urban growth and the geomorphologic features of the Bahía Blanca city and obtained that the first-order control of the LOS displacement velocity belongs to the natural topographic settings. On the other hand, the anthropogenic impact that contributes to the land subsidence sometimes is difficult to test. An example is the random buildings development distribution which in most cases does not fit with the general pattern of the LOS values. However, a combination of natural and anthropogenic impacts and mechanisms could be suggested as triggers of the land subsidence in Bahía Blanca.

The LOS displacements rates related to the land subsidence process could be originated in urban growth (generating new loads on the soil, its waterproofing and compaction), in the extraction of groundwater, and/or in the processes of soil creep associated with high topographic slopes. These factors are combined in some sectors of the city, where the highest LOS values in the area are reached. In contrast, groundwater extraction is particularly high in the northeast sector so it could be pointed as an important land subsidence contribution factor in this region additionally to the building

development impacts associated with urban growth. In this context, it is advisable to implement greater control over the growth of the Bahía Blanca city, the extraction of groundwater, and the geotechnical characteristics of the soil for the foundation to avoid negative consequences on the building and environment. This contribution points out that interferometry radar methodology provides an interesting tool that combined with geomorphological settings and human impact knowledge of any study area helps to define where are the most vulnerable areas to the land subsidence process over time.

7. Acknowledgments

We thank to CONICET and CONAE for the support to this contribution. We also thank European Space Agency (ESA) for provide Sentinel-1 images and SNAP software used in this research. We also thank to editor Dr. Bradley C. Rundquist and two anonymous reviewers for the useful comments and suggestions which lead the significant improvement of the manuscript.

References

Abidin, H. Z., Andreas, H., Gumilar, I., Sidiq, T. P., & Fukuda, Y. 2013. Land subsidence in coastal city of Semarang (Indonesia): characteristics, impacts and causes. Geomatics, Natural Hazards and Risk, 4(3), 226-240.

Albouy, R., and G. Bonorino. 1997. "Hidrogeología de la cuenca superior del río Sauce Chico, Sierras Australes, provincia de Buenos Aires." *Revista de la Asociación Geológica Argentina*, 52 (1): 81-92. URL: https://books.google.es/books?hl=es&lr=&id=R-A33RuUAiUC&oi=fnd&pg=PA81&ots=ZzU4e8pNu6&sig=p7u9xuHyKfRq6UtyuapoBnsNsnw#v=onepage&q&f=false

Albouy, R., J. Carrica, and G. Bonorino. 2005. "Identificación y análisis del fenómeno de drenaje diferido en sedimentos pampeanos. Cuenca del A°. Napostá Chico, provincia de Buenos Aires." *IV Congreso Argentino de Hidrogeología, Actas (I),* Río Cuarto, 259-268.

Benedetti, G. 1997. "Plantas sustentadoras del espacio vital bahiense." *I Jornadas Nacionales de Geografía Física. Actas,* 24: 159-165, Bahía Blanca.

Biescas, E., M. Agudo, O. Monserrat, C. Ibañez, and M. Crosetto. 2003. *Aplicaciones de la interferometría SAR para la medida de deformaciones del terreno*. Instituto de Geomática, Castelldefels, España.

Amiotti, N. and J. A. Ruiz. 2003. “Reconstrucción de la evolución geo-pedogenética en una toposecuencia del sudoeste pampeano.” *Ciencia del suelo* 21 (n.d.): 59-70. ISSN 0326-3169

Bonorino, A. G. 2005. “Acuíferos profundos e Hidrotermalismo. In Geología y Recursos Minerales de la Provincia de Buenos Aires.” *Relatorio del XVI Congreso Geológico Argentino,* XX, 327-346.

Bonorino, G, J. C. Carrica and D. Lafont. 2009. “Explotación de las aguas subterráneas para suplementar el abastecimiento a la ciudad de Bahía Blanca y zonas de influencia.” *Boletín Electrónico CONICET* - Bahía Blanca. URL: https://bahiablanca.conicet.gov.ar/boletin/boletin29/index87e4.html

Braun, A. and L. Veci. 2020. *TOPS Interferometry Tutorial. Array Systems*. URL: http://step. esa. int/docs/tutorials/S1TBX% 20TOPSAR% 20Interferometry% 20with% 20Sentinel-1% 20Tutorial_v2. pdf (accessed February 2020).

Canada Centre for Remote Sensing (CCRS). 2000. GlobeSAR2. Material educativo para teledetección mediante radares. CD, Natural Resources Canada and Canadian International Development Agency CIDA, Canada.

Carrica, J. C. 1998. “Hidrogeología de la cuenca del Arroyo Napostá Grande, Provincia de Buenos Aires.” PhD Thesis, Universidad Nacional del Sur. Bahía Blanca, Argentina.

Carrica, L., J. Carrica and E. R. Albouy. 2020. “Estado actual del conocimiento de los acuíferos en el partido de Bahía Blanca, provincia de Buenos Aires.” *Revista de Geología Aplicada a la Ingeniería y al Ambiente,* (45) 19-31. URL: https://www.editoresasagai.org.ar/ojs/index.php/rgaia/article/view/184.

Carminati, E., & Martinelli, G. 2002. Subsidence rates in the Po Plain, northern Italy: the relative impact of natural and anthropogenic causation. Engineering Geology, 66(3-4), 241-255.

Catalao, J., G. Nico, V. Conde and J. Miranda. 2012. “Quantification of Subsidence Rates Associated with Groundwater Flow Using SAR Interferometry.” *Fringe,* (697) 18. URL:

https://dragon3.esa.int/documents/10174/1576732/Quantification_subsidence_rates_groundwater_flow_SAR_interferometry.pdf

Chen, M., R., Tomás, Z. Li, M. Motagh, T. Li, L. Hu, and X. Gong. 2016. "Imaging land subsidence induced by groundwater extraction in Beijing (China) using satellite radar interferometry." *Remote Sensing*, 8 (6): 468. doi: 10.3390/rs8060468

Ciampalini, A, L. Solari, R. Giannecchini, Y. Galanti and S. Moretti. 2019. "Evaluation of subsidence induced by long-lasting buildings load using InSAR technique and geotechnical data: The case study of a Freight Terminal (Tuscany, Italy)." *International Journal of Applied Earth Observation and Geoinformation*, 82, 101925. doi: 10.1016/j.jag.2019.101925

Crosetto, M., R. Copons, M. Cuevas-González, N. Devanthéry, and O. Monserrat. 2018. "Monitoring soil creep landsliding in an urban area using persistent scatterer interferometry (El Papiol, Catalonia, Spain)." *Landslides*, 15 (7): 1317-1329. doi: 10.1007/s10346-018-0965-5.

Dang, V. K., Doubre, C., Weber, C., Gourmelen, N., and Masson, F. 2014. Recent land subsidence caused by the rapid urban development in the Hanoi region (Vietnam) using ALOS InSAR data. Natural Hazards and Earth System Sciences, 14(3), 657-674.

EO-College - European Space Agency (ESA). 2017. URL: https://eo-college.org/Data/Echoes_in_Space/Manuscripts/03_Land_Echoes_in_Space_Manuscripts.pdf

Federico, A., Popescu, M., Elia, G., Fidelibus, C., Internò, G., & Murianni, A. 2012. Prediction of time to slope failure: a general framework. Environmental earth sciences, 66(1), 245-256.

Fidalgo, F., F. De Franseco, and R. Pascual. 1975. "Geología superficial de la llanura bonaerense. In Geologia de la Provincia de Buenos Aires." *VI Congreso Geológico Argentino, Relatorio*, Bahía Blanca.

Fiorucci, F., Cardinali, M., Carlà, R., Rossi, M., Mondini, A. C., Santurri, L., Ardizzone, F., and Guzzetti, F. 2011. Seasonal landslide mapping and estimation of landslide mobilization rates using aerial and satellite images. Geomorphology, 129(1-2), 59-70.

Folguera, A., M. P. Etcheverría, M. Zárate, L. D. Escosteguy, F. Miranda, A. J. Faroux, and M. Franchi. 2017. Hoja Geológica 3963-II Bahía Blanca.

Foster, S. S. D., B. L. Morris, and P. J. Chilton. 1999. "Groundwater in urban development-a review of linkages and concerns." *IAHS PUBLICATION*, 3-12. URL: https://www.researchgate.net/profile/Stephen_Foster11/publication/280565596_Groundwater_in_urban_development_a_review_of_linkages_and_concerns/links/55b3a85608ae092e9653ac92/Groundwater-in-urban-development-a-review-of-linkages-and-concerns.pdf

Franke, D., S. Neben, B. Schreckenberger, A. Schulze, M. Stiller and C. M. Krawczyk. 2006. "Crustal structure across the Colorado Basin, offshore Argentina." *Geophysical Journal International*, 165 (3): 850-864. doi: 10.1111/j.1365-246X.2006.02907.x

FUNS - FUNDACIÓN UNIVERSIDAD NACIONAL DEL SUR. 2000. "Estudio hidrogeológico de la cuenca del A. Napostá Chico. Etapas 1, 2 y 3." Unpublished.

Gentili, J. O., M. E. Fernández, and V. Gil. 2020. "Influence of Topography on Local Atmospheric Features in a Peri-urban Area of Bahía Blanca (Argentina)." *Environmental Processes*, 7 (1): 23-40. doi: 10.1007/s40710-019-00408-4

Highland, L. and P. Bobrowsky. 2008. *The landslide handbook—a guide to understanding landslides, U.S. Geological Survey Circular 1325*, Virginia, United States. URL: https://pubs.usgs.gov/circ/1325/

Khorrami, M., Abrishami, S., Maghsoudi, Y., Alizadeh, B., and Perissin, D. 2020. Extreme subsidence in a populated city (Mashhad) detected by PSInSAR considering groundwater withdrawal and geotechnical properties. Scientific Reports, 10(1), 1-16.

Koppel, K, K. Zalite, A. Sisas, K. Voormansik, J. Praks and M. Noorma. 2015. “Sentinel-1 for urban area monitoring—Analysing local-area statistics and interferometric coherence methods for buildings' detection.” *IEEE International Geoscience and Remote Sensing Symposium (IGARSS)*, 1175-1178. doi: 10.1109/IGARSS.2015.7325981.

Koster, K., Stafleu, J., and Stouthamer, E. 2018. Differential subsidence in the urbanised coastal-deltaic plain of the Netherlands. Netherlands Journal of Geosciences, 97(4), 215-227.

Krepper, C. M., B. V. Scian and J. O. Pierini. 1989. “Time and space variability of rainfall in central-east Argentina.” *Journal of Climate*, 2 (1): 39-47. doi: 10.1175/1520-0442(1989)002%3C0039:TASVOR%3E2.0.CO;2

Listo, F. D. L. R., and B. C. Vieira. 2012. “Mapping of risk and susceptibility of shallow-landslide in the city of São Paulo, Brazil.” *Geomorphology*, 169: 30-44. doi: 10.1016/j.geomorph.2012.01.010

Liu, Q., X. Wang, and X. D. Song. 2013. “Study on Test of the Influence of Moisture Content on Creep Property of Sandy Slate Coarse-Grained Soil.” *Applied Mechanics and Materials* (405): 1733-1738. Trans Tech Publications Ltd. doi: 10.4028/www.scientific.net/AMM.405-408.1733

Lohnes, R. A., A. Millan, T. Demirel, and R. L. Handy. 1972. “Tests for Soil Creep.” *Highway Research Record*, 24-33. URL: http://onlinepubs.trb.org/Onlinepubs/hrr/1972/405/405-004.pdf

Manzo, M., G. P. Ricciardi, F. Casu, G. Ventura, G. Zeni, S. Borgstrom, P. Berardino, C. Del Gaudio, and R. Lanari. 2006. "Surface deformation analysis in the Ischia Island (Italy) based on spaceborne radar interferometry." *Journal of Volcanology and Geothermal Research*, 151 (4): 399-416. doi: 10.1016/j.jvolgeores.2005.09.010.

Morton, R. A., Buster, N. A., & Krohn, M. D. 2002. Subsurface controls on historical subsidence rates and associated wetland loss in southcentral Louisiana. Transactions Gulf Coast Association of Geological Societies, v. 52, p. 767-778.

Nagler, T., H. Rott, M. Hetzenecker, J. Wuite and P. Potin. 2015. “The Sentinel-1 mission: New

opportunities for ice sheet observations." *Remote Sensing*, 7 (7): 9371-9389. doi: 10.3390/rs70709371

Oehm, B. and B. Hallet. 2005. "Rates of soil creep, worldwide: weak climatic controls and potential feedback." *Zeitchrift fur Geomorphologie*, 49: 353-372. URL: https://www.researchgate.net/profile/B_Hallet/publication/286913942_Rates_of_soil_creep_worldwide_Weak_climatic_controls_and_potential_feedback/links/572c3dfa08ae2efbfdbde200.pdf.

Osmanoğlu, B., Dixon, T. H., Wdowinski, S., Cabral-Cano, E., and Jiang, Y. 2011. Mexico City subsidence observed with persistent scatterer InSAR. International Journal of Applied Earth Observation and Geoinformation, 13(1), 1-12.

Pawlik, Ł., and P. Šamonil. 2018. "Soil creep: The driving factors, evidence and significance for biogeomorphic and pedogenic domains and systems–A critical literature review." *Earth-Science Reviews*, 178: 257-278. doi: 10.1016/j.earscirev.2018.01.008

Peduto, D., G. Nicodemo, J. Maccabiani and S. Ferlisi. 2017. "Multi-scale analysis of settlement-induced building damage using damage surveys and DInSAR data: A case study in The Netherlands." *Engineering Geology*, 218: 117-133. doi: 10.1016/j.enggeo.2016.12.018.

Phien-Wej, N., Giao, P. H., and Nutalaya, P. 2006. Land subsidence in bangkok, Thailand. Engineering geology, 82(4), 187-201.

Poland, J. F., ed., 1984. *Guidebook to studies of land subsidence due to ground-water withdrawal*. Paris, France: UNESCO Studies and Reports in Hydrology. URL: https://hydrologie.org/BIB/Publ_UNESCO/SR_040_1984.pdf

Poreh, D., S. Pirasteh, and E. Cabral-Cano. 2021. "Assessing subsidence of Mexico City from InSAR and LandSat ETM+ with CGPS and SVM." *Geoenvironmental Disasters*, 8 (1): 1-19. doi: 10.1186/s40677-021-00179-x.

Programa de Ciudades de CIPPEC. 2017. *Hacia un plan de desarrollo urbano integral para Bahía Blanca. Una propuesta de co-creación de políticas públicas y planificacción*, Buenos Aires: CIPPEC. URL: https://www.cippec.org/wp-content/uploads/2017/09/Hacia-un-plan-de-desarrollo-urbano-integral-para-Bahia-Blanca2.pdf

Rapela, C. W. and J. Kostadinoff. 2005. "El basamento de Sierra de la Ventana: Historia tectomagmática." In De Barrio, R. E., R. O. Etcheverry, M. F. Caballé y E. Llambías (Eds): *Geología y Recursos Minerales de la provincia de Buenos Aires. 16º Congreso Geológico Argentino, Relatorio.* (V): 69-84. La Plata.

SNAP - ESA Sentinel Application Platform v2.0.2, URL: http://step.esa.int

Serco Italia SPA. 2018. Land Subsidence with Sentinel-1 using SNAP. (version 1.2). Retrieved from RUS Lectures at https://rus-copernicus.eu/portal/wp-content/uploads/library/education/training/HAZA03_Land-Subsidence_Mexico-city.pdf

Sillerico E., M. Marchamalo, J. G. Rejas, and R. Martinez. 2010. "La técnica DInSAR: bases y aplicaciones a la medición de subsidencias del terreno en la construcción." *Informes de la Construcción*. 62 (519): 47-53. doi: 10.3989/ic.09.063.

Stramondo, S., Bozzano, F., Marra, F., Wegmuller, U., Cinti, F. R., Moro, M., and Saroli, M. 2008. Subsidence induced by urbanisation in the city of Rome detected by advanced InSAR technique and geotechnical investigations. Remote Sensing of Environment, 112(6), 3160-3172.

Strozzi, T. and U. Wegmuller. 1998. "Delimitation of urban areas with SAR interferometry. In IGARSS'98. Sensing and Managing the Environment." *IEEE International Geoscience and Remote Sensing. Symposium Proceedings*. (Cat. No. 98CH36174), (3): 1632-1634. doi: 10.1109/IGARSS.1998.691660.

Teatini, P., Tosi, L., & Strozzi, T. (2011). Quantitative evidence that compaction of Holocene sediments drives the present land subsidence of the Po Delta, Italy. Journal of Geophysical Research: Solid Earth, 116(B8).

Tohver, E., P. A. Cawood, E. A Rosello. and F. Jourdan. 2012. "Closure of the Clymene Ocean and formation of West Gondwana in the Cambrian: Evidence from the Sierras Australes of the southernmost Río de la Plata craton, Argentina." *Gondwana Research,* 21: 394-405. doi: 10.1016/j.gr.2011.04.001.

Varnes, D. J., 1978. Slope movement types and processes. Special report, 176, 11-33.

Yang, Q, Y. Ke, D. Zhang, B. Chen, H. Gong, M. Lv and X. Li. 2018. "Multi-scale analysis of the relationship between land subsidence and buildings: A case study in an eastern Beijing Urban Area using the PS-InSAR technique." *Remote Sensing,* 10 (7): 1006. doi: 10.3390/rs10071006.

Zhang, Y., Liu, Y., Jin, M., Jing, Y., Liu, Y., Liu, Y., Sun, W., Wei, J., and Chen, Y. 2019. Monitoring land subsidence in Wuhan city (China) using the SBAS-InSAR method with radarsat-2 imagery data. Sensors, 19(3), 743.

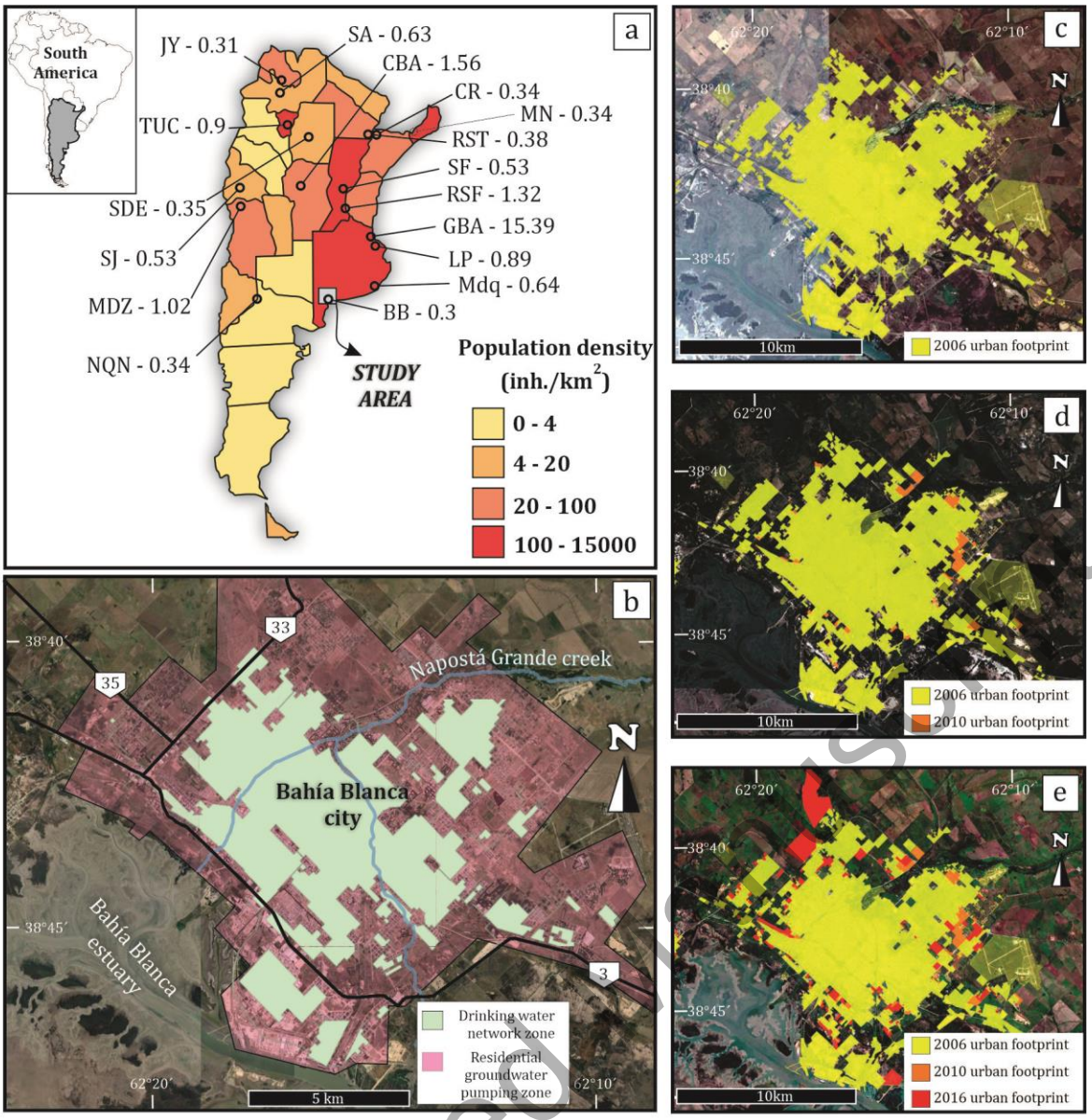

Figure 1. a) Population density map of the Argentina provinces with the location of the study area (Bahía Blanca - BB) in the southwest region of Buenos Aires Province. Black open circles show the most crowded localities of the Argentina and its estimated populations with values in millions of inhabitants: BB: Bahía Blanca; MDQ: Mar del Plata; LP: La Plata; GBA: Buenos Aires; RSF: Rosario; SF: Santa Fe; RST: Resistencia; MN: Posadas; CR: Corrientes; CBA: Córdoba; SA: Salta; JY: San Salvador de Jujuy; TUC: San Miguel de Tucuman - Tafí Viejo; SDE: Santiago del Estero; SJ: San Juan; MDZ: Mendoza; NQN: Neuquén. The population below to 0.5 million inhabitants corresponds to INDEC-2010 census and the localities with more than 0.5 million inhabitants belongs to INDEC- 2020 estimations. b) Satellite image of the study area showing the Bahía Blanca estuary, the Napostá Grande Creek, the perimeter of the Bahía Blanca city and national routes. c-e) Detail of the Bahia Blanca urban area for 2006 (c), 2010 (d) and 2016 (e) years (CIPPEC 2017).

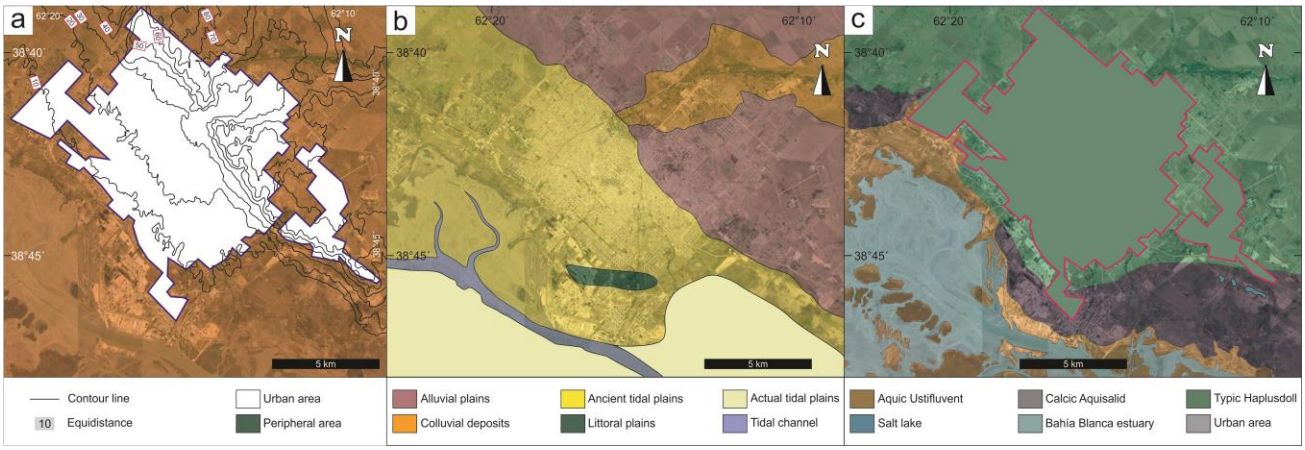

Figure 2. Topographic (a), geomorphological (b) and soil types (c) maps of the Bahía Blanca region (b and c maps modified from Folguera et al. 2017).

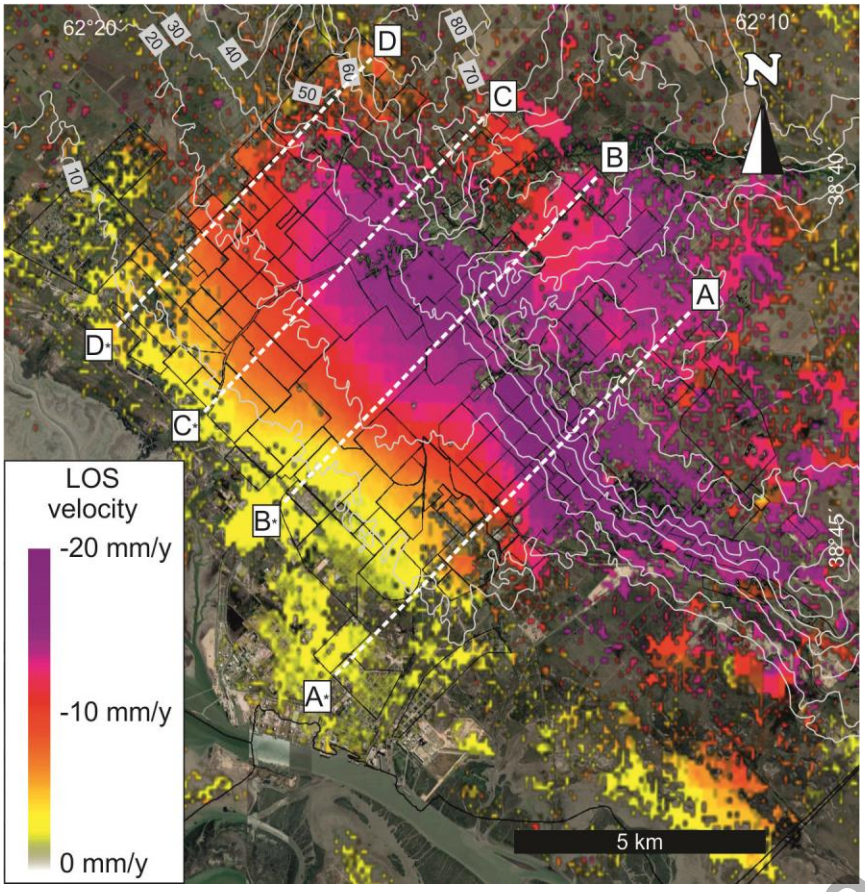

Figure 3. LOS velocity map in mm/y for the analysed period and topographic curves of the study area. Northeastern sections A*-A, B*-B, C*-C, D*-D were employed to analyse the relationship between topography and LOS displacement values (section 4.3). See the text for more details.

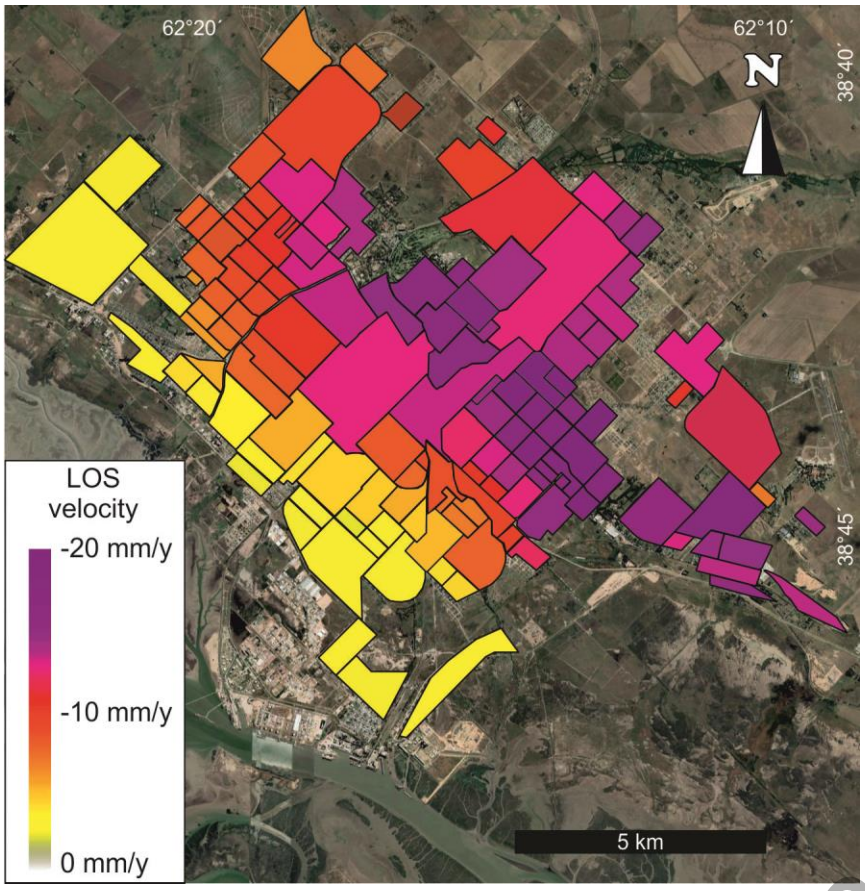

Figure 4. Mean LOS velocity map in mm/y for each neighbourhood in the analysed period. LOS velocity values are detailed in Table 2.

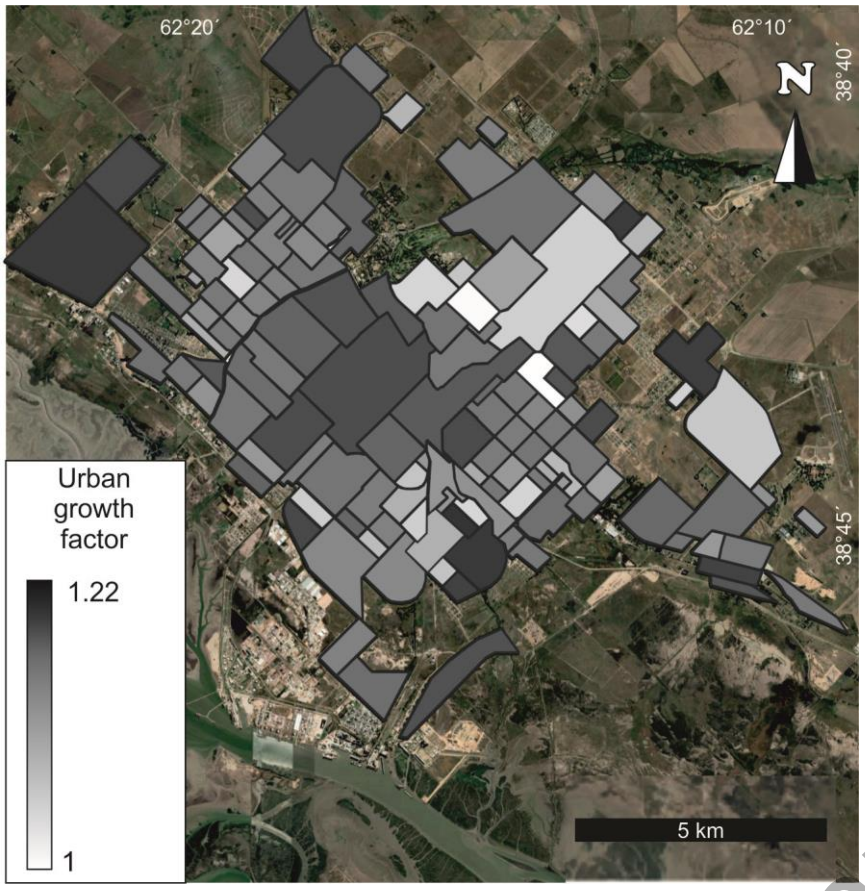

Figure 5. Urban growth factor map showing the comparison between building density in 2016 and 2020. Urban growth values for each neighbourhood are detailed in table 2.

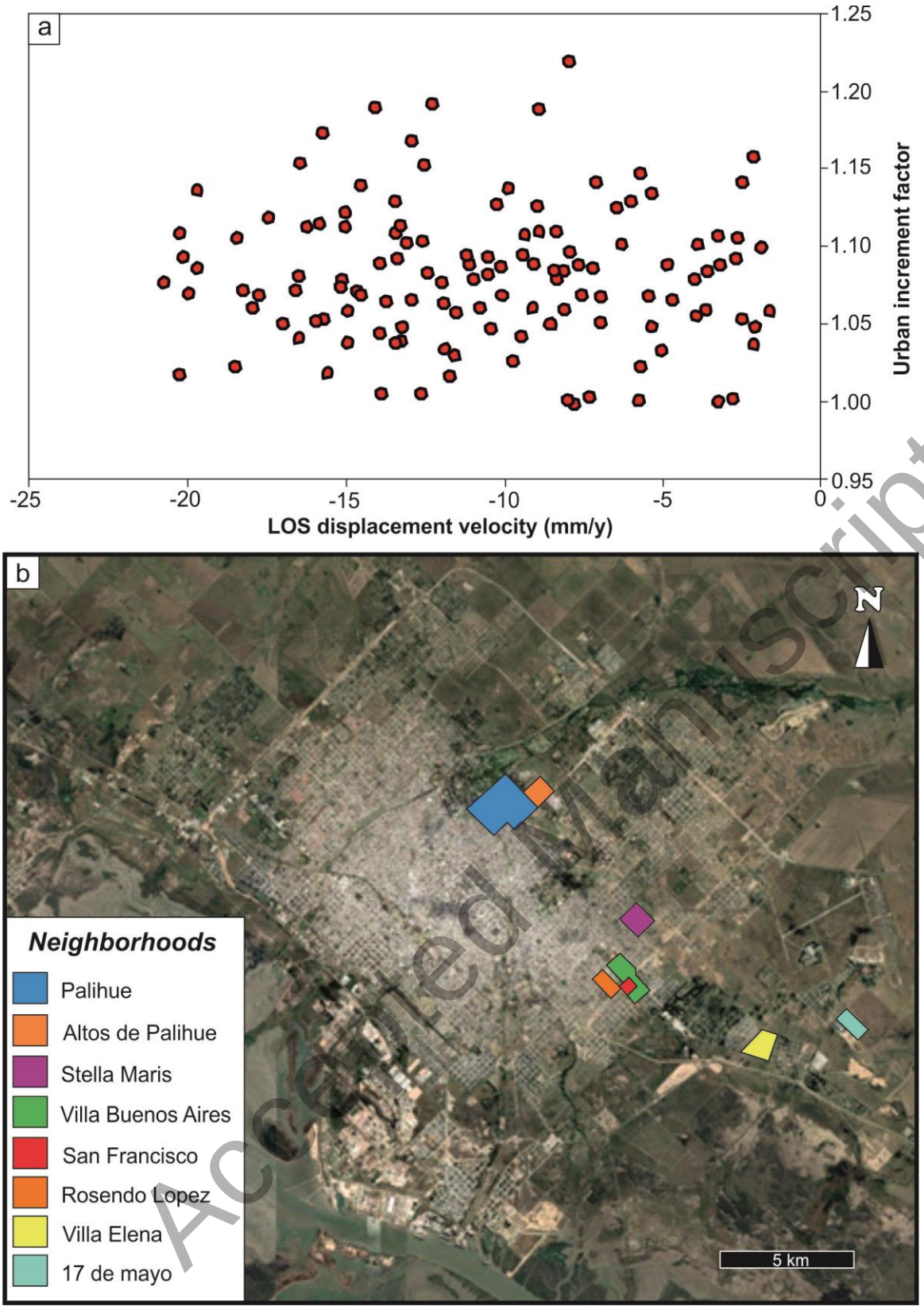

Figure 6. a) LOS velocity against urban growth factor graphic, showing a very low correlation coefficient. b) Satellite image showing the neighbourhood's location for high LOS velocity and high urban growth factor values (see table 2 for more details).

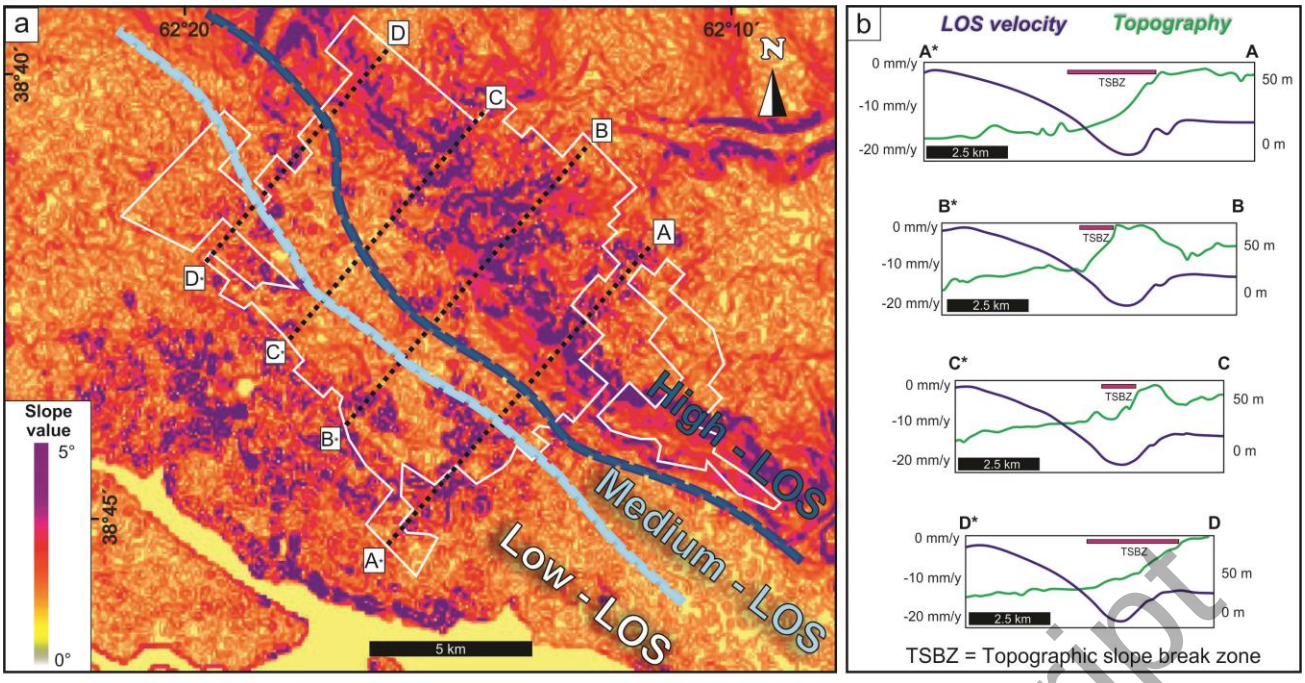

Figure 7. a) Slope map of the study area showing the location of the cross-sections A*-A, B*-B, C*-C, D*-D and the regional boundaries trend between the LOS velocity intervals (low-medium-high). b) Comparison between LOS velocity and topography over selected cross-sections. See also figure 3 for more details about the LOS values distribution and topographic characteristics of the analysed sections.

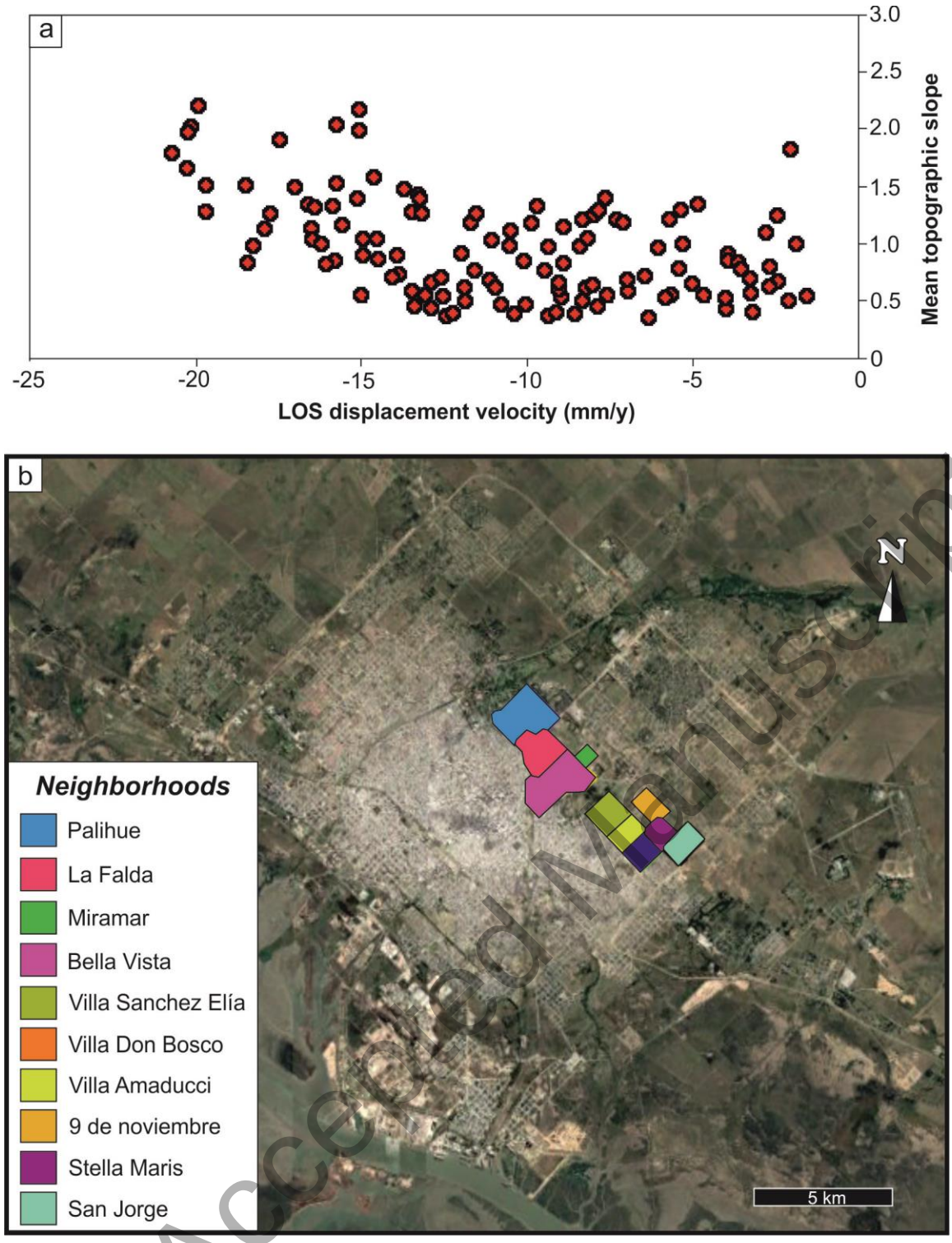

Figure 8. a) LOS velocity against Mean topographic slope, showing a low to medium correlation coefficient. b) Satellite image showing the neighbourhood's location with high LOS velocity and high topographic slope values (see table 2 for more details).

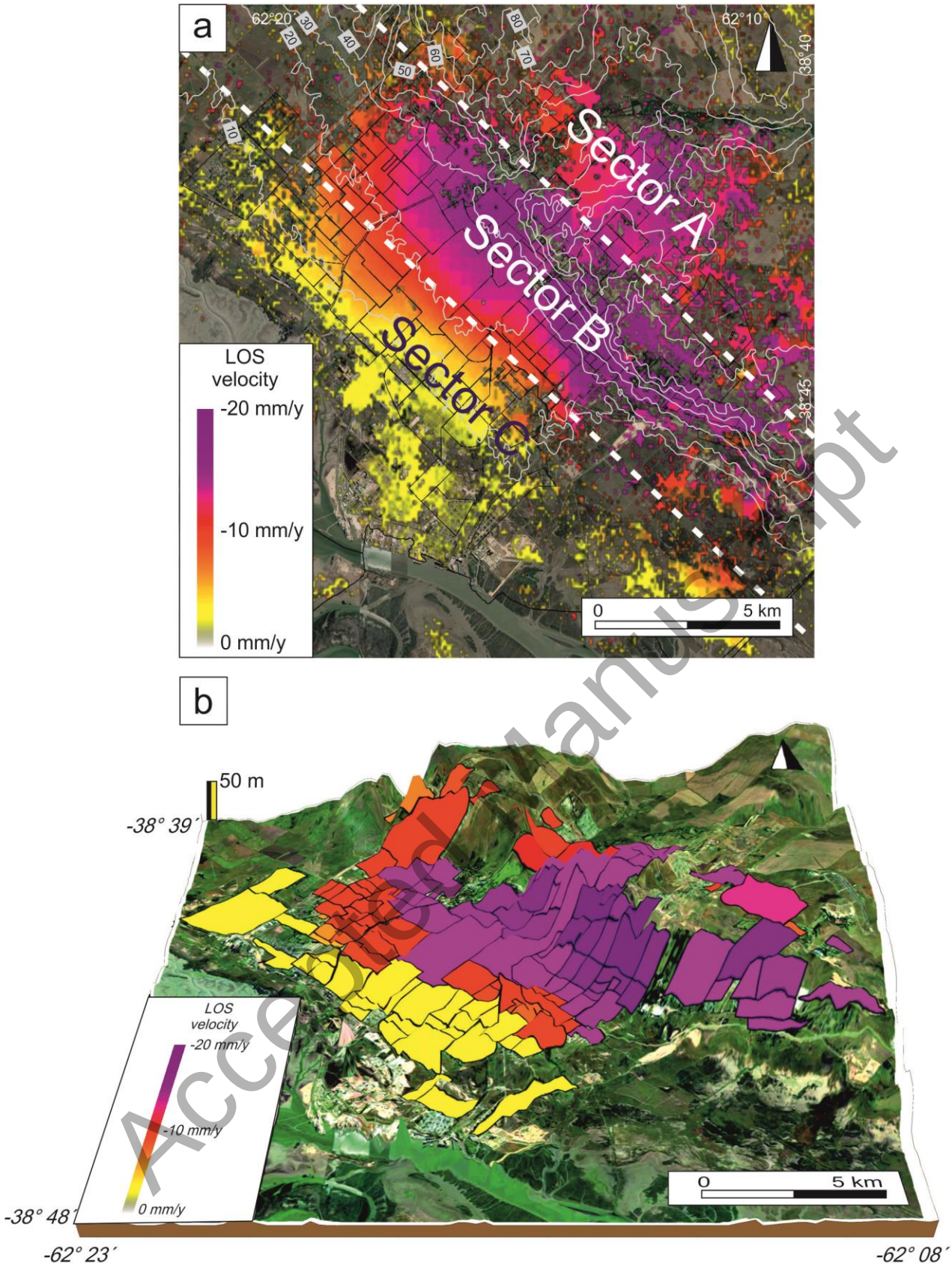

Figure 9. a) Proposed sectors of the city as a function of the LOS displacement process driving. b) 3 D model showing topography and LOS displacement by neighbourhood (vertical exaggeration x20).

Table 1. Hydrostratigraphy of the study area (Carrica et al., 2020).

Formation	Hydrostratigraphic section	Hydraulic character	Piezometric level
Maldonado	Epiparanian	Aquiclude - aquifer	Phreatic aquifer
Cerro Azul		Aquifer Aquitard - aquiclude Aquifer	Upwelling aquifer
Barranca Final	Paranian	Aquiclude - aquitard	
Ombucta	Hypoparanien	Aquiclude	
		Aquifer	Upwelling aquifer
Pedro Luro		Aquiclude	
Colorado		Aquifer	
Fortín		Aquifuge	
Basement		Aquifuge	

Table 2.. The extension (km2), LOS velocity (maximum and mean), urban grow factor (regions without growth are equal to 1,00), and mean slope (°) for each city neighbourhood.

ID	Neighborhood	Area (km^2)	Pixels inside polygon	Max LOS (mm/y)	Mean LOS (mm/y)	Urban growth factor	Mean slope (°)
1	1810	0,09	10	-7,24	-6,56	1,09	1,23
2	12 de Octubre	0,36	41	-17,47	-11,46	1,12	1,91
3	17 de Agosto	0,15	13	-12,30	-9,64	1,19	0,38
4	17 de Mayo	0,17	20	-15,02	-13,62	1,11	0,55
5	1º de Mayo	0,29	35	-5,35	-4,70	1,05	0,99
6	26 de Septiembre	0,63	71	-2,72	-1,72	1,09	0,64
7	5 de Abril	0,31	35	-11,92	-10,32	1,06	0,61
8	9 de Noviembre	0,23	18	-20,26	-19,04	1,02	1,66
9	Aerotalleres	0,25	29	-6,04	-5,40	1,13	0,97
10	Aldea Romana	3	192	-11,55	-9,19	1,06	1,24
11	Altos de Palihue	0,2	25	-16,42	-16,12	1,15	1,31
12	Avellaneda	0,65	82	-11,16	-10,05	1,10	0,67
13	Bahía Blanca	0,11	16	-18,25	-16,58	1,07	0,98
14	Barrio Anchorena	0,5	63	-14,54	-13,53	1,07	1,04
15	Barrio Obrero	0,14	18	-10,21	-9,69	1,13	0,47
16	Barrio Parque Norte	0,35	32	-9,87	-6,09	1,14	1,17
17	Barrio Parque San Miguel	1,23	87	-17,00	-14,99	1,05	1,49
18	Bella Vista	0,93	121	-14,64	-13,73	1,07	1,59
19	Bosque Alto Barrio Parque	0,53	58	-8,18	-5,21	1,06	0,61
20	Boulevard Juan B.	1,29	106	-2,16	-2,04	1,04	0,50

	Justo						
21	Caritas	0,61	60	-5,43	-1,94	1,07	0,78
22	Cecilia Larrañaga	0,07	10	-8,92	-8,34	1,11	1,15
23	Ceferino Namuncurá	0,33	42	-9,15	-8,30	1,06	0,60
24	Centro	4,27	548	-11,59	-5,32	1,03	0,77
25	Colón	0,37	47	-3,60	-2,39	1,09	0,77
26	Comandante Espora	2,81	136	-12,54	-8,81	1,15	0,55
27	Cooperación II	0,31	38	-10,12	-8,92	1,09	0,85
28	Coronel Estomba	0,37	47	-8,92	-8,17	1,19	0,85
29	Coronel Maldonado	0,6	60	-3,96	-2,85	1,06	0,85
30	Eduardo Cenci	1,22	112	-11,99	-9,80	1,08	0,91
31	El Nacional	0,3	36	-14,09	-13,30	1,19	0,70
32	El Progreso y El Porvenir	0,25	24	-7,31	-6,46	1,00	1,21
33	El Sol	0,15	12	-10,52	-8,09	1,09	1,12
34	Enrique Julio	0,34	22	-2,16	-1,47	1,16	1,84
35	Gral. Arias	0,19	19	-2,10	-1,47	1,05	1,82
36	Grünbein	0,56	65	-16,59	-14,02	1,07	1,35
37	Independencia Altos	0,75	66	-16,50	-13,04	1,04	1,04
38	Juan López	0,25	30	-7,14	-5,69	1,14	1,20
39	Kilómetro 5	0,75	95	-8,37	-7,35	1,08	0,50
40	La Falda	0,65	83	-15,74	-14,83	1,05	1,53

41	La Piedad	1,46	183	-5,05	-2,59	1,03	0,65
42	Las Acacias	0,58	55	-13,08	-11,41	1,10	0,55
43	Las Lomitas	1,24	56	-8,02	-2,05	1,00	1,25
44	Latino	0,48	57	-9,00	-8,24	1,13	0,54
45	Loma Paraguaya	0,43	48	-2,80	-1,89	1,00	1,09
46	Los Álamos	0,06	8	-6,48	-5,40	1,13	0,71
47	Los Almendros	0,41	52	-10,07	-9,15	1,07	0,47
48	Los Chañares	1,3	84	-5,70	-1,79	1,02	0,54
49	Los Horneros	0,41	51	-14,53	-13,23	1,14	0,86
50	Los Muñecos	1,18	84	-10,56	-8,47	1,08	0,98
51	Los Teritos	0,06	8	-11,72	-11,29	1,02	1,17
52	Luján	0,31	41	-7,92	-7,25	1,10	0,46
53	Mara	0,25	34	-6,34	-5,51	1,10	0,35
54	Mariano Moreno	0,84	109	-6,96	-5,65	1,05	0,59
55	Mi Casita	0,23	25	-9,50	-8,49	1,04	0,77
56	Milla Mapu	0,54	67	-13,93	-12,70	1,09	0,72
57	Miramar	0,14	13	-15,09	-13,84	1,07	2,17
58	Napostá	0,77	97	-14,94	-14,36	1,04	1,05
59	Nueva Belgrano	0,68	74	-9,05	-7,29	1,09	0,66
60	Oasis	0,27	31	-17,75	-14,41	1,07	1,27
61	Obrero	0,94	105	-1,64	-0,72	1,06	0,53
62	Pacífico	1,61	208	-10,41	-8,33	1,05	0,39
63	Palermo	0,45	38	-15,59	-11,72	1,02	1,17
64	Palihue	0,96	121	-15,73	-15,08	1,17	2,04
65	Palos Verdes	1,32	123	-15,06	-11,19	1,12	1,99
66	Pampa Central	1,06	133	-4,72	-2,64	1,07	0,55

67	Patagonia	3,98	463	-13,27	-11,03	1,12	1,39
68	Patagonia Norte	0,34	42	-13,86	-13,18	1,01	0,74
69	Pedro Pico	1,07	137	-8,58	-5,80	1,05	0,39
70	Portal del Este	0,46	15	-15,13	-13,37	1,08	1,40
71	Prensa	0,59	65	-13,50	-11,96	1,13	1,28
72	Punta Blanca	0,26	16	-13,33	-7,63	1,04	1,42
73	Ricchieri	0,32	41	-7,59	-6,62	1,07	0,55
74	Rivadavia	0,57	69	-8,35	-6,12	1,11	1,21
75	Rosario Sur	0,6	70	-9,36	-8,20	1,11	0,98
76	Rosendo López	0,12	15	-15,83	-15,16	1,12	0,85
77	Rucci	0,19	25	-2,49	-1,55	1,14	0,66
78	S.O.S.B.A	0,21	14	-8,13	-7,43	1,08	1,04
79	San Blas	0,4	39	-3,29	-2,35	1,11	0,69
80	San Cayetano	0,59	73	-12,93	-11,48	1,07	0,44
81	San Francisco	0,06	7	-18,44	-17,95	1,11	0,83
82	San Ignacio	0,35	44	-13,73	-12,82	1,07	1,47
83	San Jorge	0,41	38	-18,52	-13,44	1,02	1,52
84	San Martín	1,4	169	-3,65	-1,40	1,06	0,83
85	San Roque	0,3	38	-10,97	-9,93	1,08	0,62
86	San Vicente	0,14	13	-9,35	-4,40	1,09	0,37
87	Sesquicentenario	0,28	34	-8,43	-7,14	1,08	0,98
88	Solares Norte	0,19	22	-11,11	-7,40	1,09	1,03
89	Spurr	0,2	18	-5,74	-4,16	1,15	1,22
90	Stella Maris	0,22	19	-20,23	-17,74	1,11	1,97
91	Thompson	0,23	27	-8,00	-6,89	1,22	0,66
92	Tiro Federal	2,28	248	-13,23	-9,85	1,05	1,28

93	U.O.M	0,26	32	-6,97	-6,16	1,07	0,69
94	U.P.C.N	0,46	58	-5,39	-3,89	1,14	1,29
95	Universitario	1,45	186	-13,44	-11,89	1,04	0,45
96	Villa Aeropuerto	1,37	85	-15,88	-9,37	1,05	1,33
97	Villa Amaducci	0,33	44	-20,17	-18,63	1,09	2,02
98	Villa Belgrano	3,38	273	-9,72	-4,61	1,03	1,33
99	Villa Bordeu y Don Ramiro	4	230	-3,28	-1,55	1,00	0,57
100	Villa Buenos Aires	0,29	36	-19,68	-18,28	1,14	1,28
101	Villa Caracol	0,35	28	-2,50	-1,32	1,05	1,25
102	Villa Centenario	0,3	31	-4,88	-3,95	1,09	1,34
103	Villa Cerrito	0,71	89	-19,94	-18,82	1,07	2,21
104	Villa del Parque	0,46	60	-13,40	-11,82	1,09	0,55
105	Villa Delfina	1,69	166	-1,92	-1,91	1,10	0,99
106	Villa Don Bosco	0,34	41	-20,74	-20,03	1,08	1,80
107	Villa Duprat	0,19	22	-9,09	-4,90	1,09	0,41
108	Villa Elena	0,24	29	-16,23	-14,80	1,11	0,99
109	Villa Floresta	1,09	131	-13,93	-13,06	1,05	0,90
110	Villa Gloria	0,15	19	-16,01	-14,84	1,05	0,84
111	Villa Harding Green	1,14	101	-12,61	-8,29	1,01	0,70
112	Villa Irupé	0,41	48	-7,67	-6,55	1,09	1,38
113	Villa Italia	0,45	56	-12,93	-10,17	1,17	0,66
114	Villa Libre	0,33	42	-16,47	-14,07	1,08	1,13
115	Villa Libre Sur	0,34	43	-17,95	-15,05	1,06	1,13
116	Villa Loreto	0,33	43	-13,45	-11,34	1,11	0,58

117	Villa Mitre	0,82	106	-11,89	-9,66	1,03	0,50
118	Villa Moresino	1,11	76	-7,82	-5,04	1,00	1,31
119	Villa Muñiz	0,77	87	-14,96	-11,77	1,06	0,90
120	Villa Nocito	0,34	40	-3,94	-2,88	1,10	0,89
121	Villa Nueva	0,17	21	-10,78	-9,52	1,06	0,46
122	Villa Parodi	0,32	40	-3,20	-2,44	1,09	0,40
123	Villa Ressia	0,64	81	-4,01	-2,02	1,08	0,44
124	Villa Rosas	1,1	136	-2,68	-1,44	1,11	0,80
125	Villa Sánchez Elia	0,43	53	-19,70	-15,02	1,09	1,50
126	Villa Santa Margarita	0,44	57	-12,61	-11,53	1,10	0,63
127	Villa Serra	0,26	29	-5,77	-4,07	1,00	0,54
128	Villa Soldati	0,37	48	-12,45	-10,58	1,08	0,37